Monthly Notices of the ROYAL ASTRONOMICAL SOCIETY

MNRAS **535,** 1625–1639 (2024) https://doi.org/10.1093/mnras/stae2442
Advance Access publication 2024 October 25

Survey of gravitationally lensed objects in HSC imaging (SuGOHI) – X. Strong lens finding in the HSC-SSP using convolutional neural networks

Anton T. Jaelani [1,2★] Anupreeta More [3,4] Kenneth C. Wong [5,6] Kaiki T. Inoue [7] Dani C.-Y. Chao,[8] Premana W. Premadi[1] and Raoul Cañameras[9,10]

[1]*Astronomy Research Group and Bosscha Observatory, FMIPA, Institut Teknologi Bandung, Jl. Ganesha 10, Bandung 40132, Indonesia*
[2]*U-CoE AI-VLB, Institut Teknologi Bandung, Jl. Ganesha 10, Bandung 40132, Indonesia*
[3]*Inter-University Centre for Astronomy and Astrophysics (IUCAA), Ganeshkhind, Pune 411007, India*
[4]*Kavli Institute for the Physics and Mathematics of the Universe (WPI), The University of Tokyo, 5-1-5 Kashiwanoha, Kashiwa, Chiba 277-8583, Japan*
[5]*Research Center for the Early Universe, Graduate School of Science, The University of Tokyo, 7-3-1 Hongo, Bunkyo-ku, Tokyo 113-0033, Japan*
[6]*National Astronomical Observatory of Japan, 2-21-1 Osawa, Mitaka, Tokyo 181-8588, Japan*
[7]*Department of Physics, Kindai University, 3-4-1 Kowakae, Higashi-Osaka, Osaka 577-8502, Japan*
[8]*Ruđer Bošković Institute, Bijenička cesta 54, 10000 Zagreb, Croatia*
[9]*Max-Planck-Institut für Astrophysik, Karl-Schwarzschild-Str. 1, D-85748 Garching, Germany*
[10]*Department of Physics, TUM School of Natural Sciences, Technical University of Munich, James-Franck-Str. 1, D-85748 Garching, Germany*

Accepted 2024 October 22. Received 2024 September 30; in original form 2023 December 12

ABSTRACT

We apply a novel model based on convolutional neural networks (CNN) to identify gravitationally lensed galaxies in multiband imaging of the Hyper Suprime-Cam Subaru Strategic Program (HSC-SSP) Survey. The trained model is applied to a parent sample of 2350 061 galaxies selected from the $\sim$ 800 deg^2 Wide area of the HSC-SSP Public Data Release 2. The galaxies in HSC Wide are selected based on stringent pre-selection criteria, such as multiband magnitudes, stellar mass, star formation rate, extendedness limit, photometric redshift range, etc. The trained CNN assigns a score from 0 to 1, with 1 representing lenses and 0 representing non-lenses. Initially, the CNN selects a total of 20 241 cutouts with a score greater than 0.9, but this number is subsequently reduced to 1522 cutouts after removing definite non-lenses for further visual inspection. We discover 43 grade A (definite) and 269 grade B (probable) strong lens candidates, of which 97 are completely new. In addition, we also discover 880 grade C (possible) lens candidates, 289 of which are known systems in the literature. We identify 143 candidates from the known systems of grade C that had higher confidence in previous searches. Our model can also recover 285 candidate galaxy-scale lenses from the Survey of Gravitationally lensed Objects in HSC Imaging (SuGOHI), where a single foreground galaxy acts as the deflector. Even though group-scale and cluster-scale lens systems are not included in the training, a sample of 32 SuGOHI-c (i.e. group/cluster-scale systems) lens candidates is retrieved. Our discoveries will be useful for ongoing and planned spectroscopic surveys, such as the Subaru Prime Focus Spectrograph project, to measure lens and source redshifts in order to enable detailed lens modelling.

Key words: gravitational lensing: strong – methods: data analysis – catalogues – surveys.

1 INTRODUCTION

As strong gravitational lensing systems are discovered over large cosmological volume, they are powerful astrophysical tools to refine cosmological models and study the evolution of cosmic large-scale structures. Studies of strong lens systems have been successfully used to probe the total mass distribution (including both baryonic and dark matter) from galaxy (e.g. Koopmans et al. 2006; Auger et al. 2010; Sonnenfeld et al. 2015; Shajib et al. 2021) to group and cluster scales (e.g, Limousin et al. 2009; More et al. 2012; Oguri et al. 2012; Newman et al. 2013; Jauzac et al. 2021; Allingham et al. 2023), constrain dark matter substructures (e.g. Vegetti et al. 2010, 2012; Hezaveh et al. 2016; Inoue et al. 2016; Nierenberg et al. 2017; Gilman et al. 2020; Hsueh et al. 2020; Inoue et al. 2023), and study compact high-redshift objects in detail by overcoming the sensitivity and/or resolution limits of current facilities by exploiting the lensing magnification effect (e.g. Marques-Chaves et al. 2017; More et al. 2017; Jaelani et al. 2020b). Moreover, strongly lensed quasars with time delay measurements can be used to test the cosmological model by constraining cosmological parameters such as the Hubble constant (e.g. Refsdal 1964; Birrer et al. 2020; Wong et al. 2020).

In the last decade, deep learning has led to very good performance on a variety of problems, such as visual recognition, speech recognition, and natural language processing, including the application in astrophysical problems, for example, strong gravitational lensing detection. Among different types of deep neural networks,

★ E-mail: antontj@itb.ac.id

convolutional neural networks (CNNs) have been most extensively studied. Lecun et al. (1998) published the seminal paper establishing the improved modern framework of CNNs. The CNNs can learn to extract information from large amounts of labelled data without explicitly defining features, making them appealing for a wide range of physical problems where hand-crafted descriptors are typically used to analyse data. It captures the essence of images using translation-invariant sliding window filter matching algorithms. The CNNs have proven extremely efficient as 'state of the art' for pattern recognition tasks and have given a strong impetus to image analysis and processing. Recent studies largely demonstrate the ability of supervised CNNs to identify the rare gravitational lenses among large data sets (e.g. Jacobs et al. 2017, 2019; Petrillo et al. 2019; Cañameras et al. 2020; Huang et al. 2021; Li et al. 2021; Zaborowski et al. 2023), extending previous automated algorithms (e.g. Gavazzi et al. 2014) generally with better classification performance (Metcalf et al. 2019).

The Survey of Gravitationally lensed Objects in HSC Imaging (SuGOHI) is an ongoing lens search that aims to discover a large number of strong gravitational lens systems from the large homogeneous data of the Hyper Suprime-Cam Subaru Strategic Program (HSC-SSP). SuGOHI has discovered about 2000 strong gravitational lens candidates at both the galaxy-scale (SuGOHI-g; Sonnenfeld et al. 2018; Wong et al. 2018, 2022; Sonnenfeld et al. 2020), and the galaxy group/cluster-scale (SuGOHI-c; Jaelani et al. 2020b), including a number of lensed quasar candidates (SuGOHI-q; Chan et al. 2020, 2023; Jaelani et al. 2021). These lenses were discovered using a variety of search techniques, including semi-automated algorithms, visual inspection, and citizen science (see summary in Table 1). In this work, we apply a CNN to identify new strong gravitational lens systems. Cañameras et al. (2021) and Shu et al. (2022) have independently applied machine learning-based lens search algorithms with different networks to the HSC SSP Public Data Release 2 (PDR2) (Aihara et al. 2019) and published lens candidates produced by these searches. SuGOHI lens candidates, specifically galaxy-scale lenses, can be used as test samples because previous searches overlapped the sky area used in this work.

The paper is organized as follows. First, in Section 2, we provide a brief overview of the HSC-SSP PDR2 and the definition of our parent sample. In Section 3, the system of simulated lenses is described. In Section 4, we discuss the networks, training procedures, CNN's performance, and visual inspection. Section 5 presents new lens candidates. Discussions and conclusions are presented in Section 6. Throughout this paper, we adopt a Hubble constant of $H_0 = 72\,\mathrm{km\ s^{-1}\,Mpc^{-1}}$, and cosmological density parameters of $\Omega_\mathrm{M} = 0.26$ and $\Omega_\Lambda = 0.74$. The AB system is used for all magnitudes. All images are oriented with North up and East to the left.

2 THE HSC-SSP PDR2

The HSC-SSP Survey is an optical imaging survey conducted with the HSC (Coupon et al. 2018; Furusawa et al. 2018; Huang et al. 2018; Kawanomoto et al. 2018; Komiyama et al. 2018; Miyazaki et al. 2018), a 1.7 deg^2 field-of-view optical camera on the 8.2-m *Subaru telescope*, which has a pixel scale of 0.168 arcsec pixel^{-1}. In this work, we use data products from the HSC-SSP PDR2 Wide covering $\sim 800\,\mathrm{deg^2}$ (Aihara et al. 2019) in *gri* bands out of a final survey area of 1400 deg^2. The median 5σ depths (for point sources) in *gri* filters for the PDR2 Wide layer are 26.6, 26.2, and 26.2 mag, while the median seeings are 0.77, 0.76, and 0.58 arcsec, for *gri*, respectively. The PDR2 data is processed with `hscPipe` version 6 (Bosch et al. 2018). Aihara et al. (2019) use a variety of aperture sizes for PDR2 photometric measurements, but a small aperture (e.g. 1.5 arcsec) is recommended to avoid blending with nearby sources. They note that the aperture corrections (Bosch et al. 2018) based on unresolved point sources have been applied to those aperture fluxes, allowing users to obtain meaningful colours. The combination of a large area and observation depth makes the data from the HSC-SSP Survey ideal for discovering new or unusual strong gravitational lenses (e.g. HSC J090429.75-010228.2; Jaelani et al. 2020a).

The photometric redshifts used in this work are determined using the `mizuki` algorithm (Tanaka 2015). The robustness of the photometric redshifts is a function of galaxy redshift and brightness, and is quantified in terms of $\Delta z/(1+z_\mathrm{ref})$, where $\Delta z \equiv |z - z_\mathrm{ref}|$ and z_ref is a reference redshift. The `mizuki`'s photometric redshifts measurement are most accurate at $0.2 \lesssim z_\mathrm{phot} \lesssim 1.5$. A thorough explanation of `mizuki`'s application to the HSC-SSP data is presented in Tanaka et al. (2018). Since the HSC-SSP Survey footprint overlaps with the Sloan Digital Sky Survey (SDSS), we collect spectroscopic redshifts, whenever available, from the SDSS Data Release 16 (Ahumada et al. 2020) catalogues.

For our strong lens search, we select to be our parent sample galaxies in PDR2 Wide retrieved from the HSC CAS Search service[1] based on their magnitude limit, stellar mass, and star formation rate. To be more specific, we select objects from tables that satisfy the following criteria:

(i) for `pdr2_wide.forced`
  (a) `isprimary` is `True`
  (b) `[grizy]_pixelflags_edge` is `False`
  (c) `[grizy]_pixelflags_interpolatedcenter` is `False`
  (d) `[grizy]_pixelflags_crcenter` is `False`
  (e) `[grizy]_cmodel_flag` is `False`
  (f) `i_extendedness_value` > 0.9
  (g) `([ri]_cmodel_mag−a_[ri])` < 28.0
  (h) `(z_cmodel_mag−a_z)` < 23.0

(ii) for `pdr2_wide.forced2`
  (i) `[grizy]_sdsscentroid_flag` is `False`

(iii) `pdr2_wide.meas`
  (j) `[grizy]_inputcount_value` > 0

(iv) `pdr2_wide.masks`
  (k) `i_mask_pdr2_bright_objectcenter` is `False`

(v) `pdr2_wide.photoz_mizuki`
  (l) 0.2 < `photoz_median` < 1.2
  (m) `stellar_mass` > 5.0e10
  (n) `(sfr/stellar_mass)` < 1.0e-10.

We remove objects with saturated pixels and unreliable photometry, as well as probable stars, using criteria 2–11. We concentrate on finding lensed features among a set of galaxies based on the properties that make them possible lenses, as defined by criteria 12–14. The upper redshift and lower stellar mass bounds are a compromise between obtaining a sample of lenses as complete as possible and the need to find lenses with Einstein radius smaller than 1 arcsec. The lower redshift cut is introduced to avoid dealing with

[1] https://hsc-release.mtk.nao.ac.jp/datasearch/

Table 1. Summary of previous SuGOHI lens searches.

SuGOHI	Data release	Area (deg^2)	Inspected objects	Grades (A, B, C)	Description
I	Up to S16A	442	$\sim$ 43 000 (LRG)	(15, 36, 282)	YattaLens[a], Chitah[b], Spectroscopic
II	Up to S17A	776	31 286 (LRG)	(7, 34,...)	YattaLens[a]
IV	Up to S16A	456	$\sim$ 45 000 (LRG); $\sim$ 110 000 (QSO)	(17, 26,...)	Chitah[b]
V	Up to S18A	1114	$\sim$ 39 500 (Galaxy clusters)	(47, 181, 413)	Cluster catalogues, Human-inspection
VI	Up to S16A	442	$\sim$ 300 000	(14, 129, 581)	Citizen-Scientist
VII	–	–	SQLS; *Chandra* catalogue	(3,...,...)	reinspection previous catalogues
VIII	Up to S21A	1310	103 191 (LRG)	(8, 28, 138)	YattaLens[a]
IX	Pp to S21A	1310	1652 329 (Quasar)	(73, 17, 53)	Colour similarity, YattaLens[a]

Notes. [a]I (Sonnenfeld et al. 2018); II (Wong et al. 2018); IV (Chan et al. 2020); V (Jaelani et al. 2020b); VI (Sonnenfeld et al. 2020); VII (Jaelani et al. 2021); VIII (Wong et al. 2022); IX (Chan et al. 2023); [b](Chan et al. 2015). LRG is luminous red galaxies, QSO is quasi-stellar objects, and SQLS is Sloan Digital Sky Survey Quasar Lens Search. The SuGOHI database has around 2000 lens candidates ($\sim$ 800 are grades A and B) from previous searches.

Table 2. Thresholds used in the selection of the simulated lenses.

Parameter	Range	Unit
Lens (SIE)		
Einstein radius, θ_E	[0.5, 3.0]	arcsec
Redshift, $z_{\ell,\mathrm{phot}}$	[0.2, 1.1]	–
External shear, γ_{ext}	[0.001, 0.020]	
PA of external shear, $\phi_{\gamma_{\mathrm{ext}}}$	[0, 180]	degree
Source		
Redshift, z_s	[1.2, 4.0]	–
i-magnitude, $m_{i,s}$	[23, 26]	–
Ellipticity, e_s	[0.1, 0.8]	–
PA of Ellipticity, ϕ_{e_s}	[0, 180]	degree

galaxies that are too bright for the detection of lensed features, which are typically faint. This query returns a total of 2350 061 unique HSC objects. We use HSC *gri* cutouts (64 $\times$ 64 pixel^2 corresponding to 10.752$\times$ 10.752 arcsec^2, which is sufficient for galaxy-scale lenses) centred on the parent objects, which are retrieved from the PDR2 Image Cutout service[2]

3 SIMULATED GALAXY-SCALE LENSES

In order to train the network on a large sample of realistic galaxy-scale lenses, we use the SIMCT[3] pipeline (detailed in More et al. 2016). With this pipeline, we superpose a set of simulated lensed galaxies on the real image cutouts of massive galaxies from the multiband HSC imaging (see Section 2). This ensures that most of the features and properties in the training images will statistically be similar to the real survey images which will be classified. The methodology of SIMCT is summarized below.

The mass model of the lens galaxies is assumed to follow singular isothermal ellipsoid (SIE, Kormann, Schneider & Bartelmann 1994) and the contribution from an external shear is also included in the model (see Table 2). We start with the position, photometric magnitudes, photometric redshifts, and ellipticity of the massive galaxies to convert their light parameters into the SIE model mass parameters. Thus, following the $L-\sigma_v$ scaling relation (Parker et al. 2005), we obtain the velocity dispersion. Similarly, assuming mass follows light, we obtain the position of the lens potential and the ellipticity parameters. We use adaptive moments (which use an elliptical Gaussian weighting function) from the PDR2 catalogue to measure lens ellipticities and position angles (PAs). Then, the Einstein radius, θ_E, with an axis ratio, $q = 1 - e$, and its dependence on the velocity dispersion of the SIE is given by

$$\theta_E = 4\pi \sqrt{\frac{2q}{1+q^2}} \left(\frac{\sigma_v}{c}\right)^2 \frac{D_{\mathrm{ls}}}{D_{\mathrm{s}}}, \quad (1)$$

where D_{ls}, D_{s}, and c are the angular diameter distance between the lens and the source, the angular diameter distance between the observer and the source, and the speed of light, respectively.

The i-band magnitude and the redshift of the background galaxies are drawn from the source counts and redshift distribution as prescribed in Faure et al. (2009). Faure et al. assumed that the number density of sources at redshift z_s brighter than the apparent magnitude threshold of $m_{\mathrm{lim}} \sim 26$ [mag] in the *F814W* filter band. Each galaxy is parameterized with a Sersic profile for a fixed Sersic index of 1 corresponding to an exponential profile. The ellipticity and PA are drawn randomly from a uniform distribution within the range indicated in Table 2. The colours of the galaxy are extracted from the photometric CFHTLenS catalogue (Hildebrandt et al. 2012; Erben et al. 2013). The effective radius of the galaxy is estimated from the luminosity−size ($L-r_{\mathrm{eff}}$) relation (Bernardi et al. 2003, with a redshift scaling to account for size evolution) given by

$$r_{\mathrm{eff}} = 10^{0.52} \frac{L_r^{2/3}}{(1+z_{\mathrm{s}})^2} \ \mathrm{kpc}, \quad (2)$$

where $L_r = L_{\mathrm{s}}/10^{10.2}\,\mathrm{L}_\odot$ and L_{s} is the luminosity of background source.

Given the source and the lens population properties, as above, we compute the probability of lensing by following (More et al. 2016, see their section 3.1.1) which accounts for the lensing cross-section, their number densities and magnification bias. Here, we limit a massive galaxy to act as a lens and accept a background source if the Einstein radius falls within the range given in Table 2 and the magnitude of the second brightest lensed image is above the limiting magnitude of the HSC Survey. Once all of the parameters for the lens and source models have been determined, we use GRAVLENS (Keeton 2001) to generate simulated lensed images. After accounting for the shot noise in the lensed images and convolving them with the seeing in each of the filters. The simulated lensed image is added to the real HSC image centred on the galaxy selected to act as a lens (see the left panel in Fig. 1). Fig. 2 shows the distributions of the Einstein radius, redshifts, i-band magnitude, and ellipticity for both lens and the source of the simulated galaxy-scale lenses. We also show the distribution of colour–colour ($m_r - m_i$ versus $m_g - m_r$) diagram of the lens galaxies and the sources (see Fig. 3) with selection effect

[2]https://hsc-release.mtk.nao.ac.jp/das_cutout/pdr2/
[3]https://github.com/anupreeta27/SIMCT

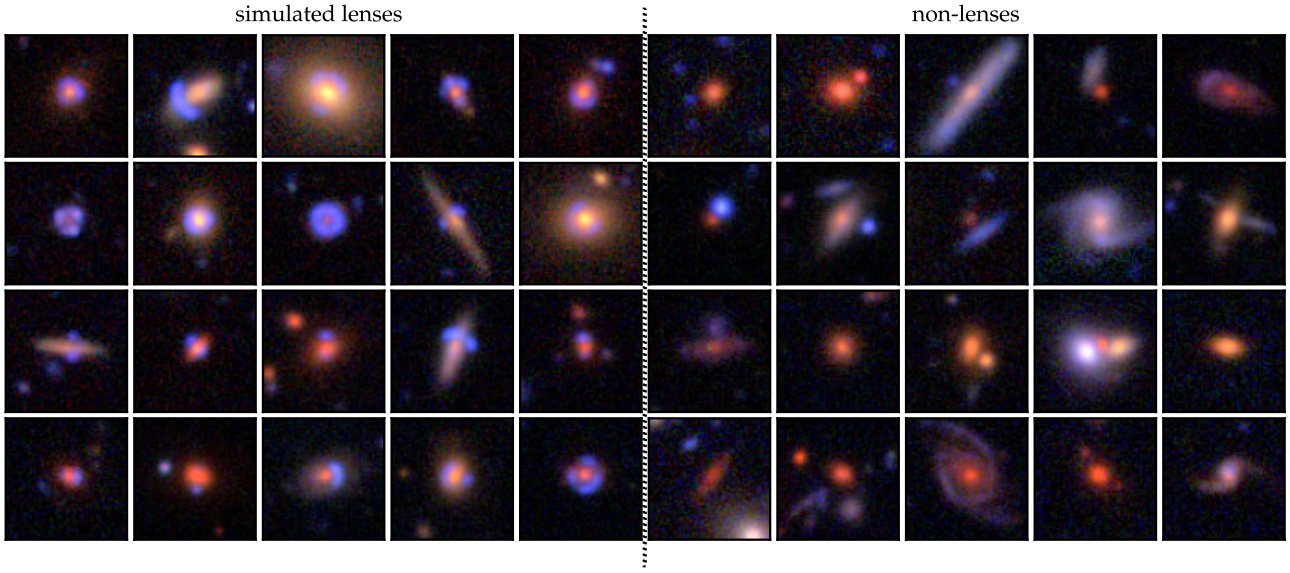

Figure 1. Left panel: examples of simulated lenses based on real HSC SSP colour composite images. Right panel: examples of objects used as non-lenses during the training of the CNN. All postage stamps are 64 pixels on a side, corresponding to 10.752 arcsec.

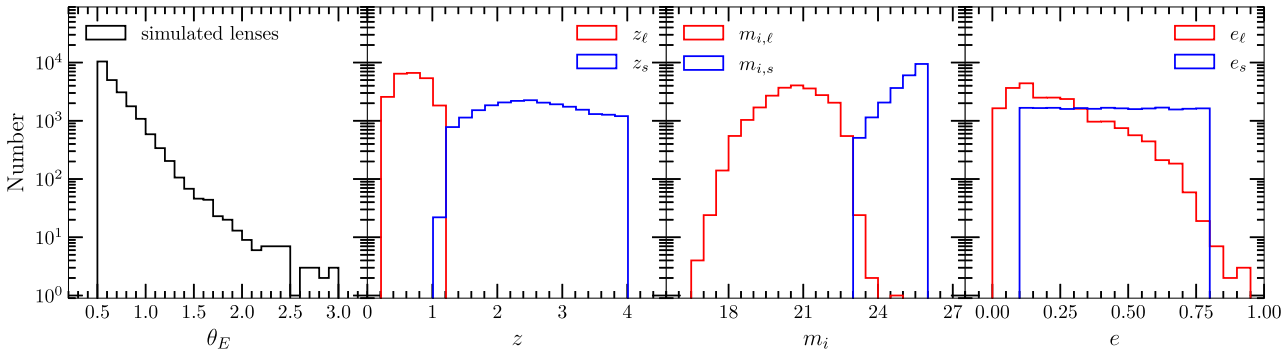

Figure 2. The distribution of the properties of the simulated lenses is constructed by SIMCT. Left to right panels: the Einstein radius, θ_E; the redshift, z; the i-band magnitude, m_i; and the ellipticity, e.

tend to bluer sources.

From a total of about 22 000 simulated lens systems, we exclude about 3000 systems located within GAMA09H field which is used for a comparison analysis in More et al. (2024). We also exclude tens of simulated lens galaxies whose centres have been identified as known lens galaxies in previous studies (e.g. More et al. 2012; Sonnenfeld et al. 2018, 2020). We then end up with 18 660 simulated lens systems.

4 CONVOLUTIONAL NEURAL NETWORK

4.1 Training data set

The data set for training the CNN is divided into two subsets of equal number of members: one containing the 18 660 simulated lenses simulated with 64 × 64 pixel (corresponding to 10.752 × 10.752 arcsec^2) cutouts from Section 3, and the other containing the 18 660 non-lens objects that were not used to generate simulated lenses. These cutouts are large enough to capture galaxy-scale lenses and yet small enough for fairly quick training and searching.

The data set is split into 80 per cent for training and 20 per cent for validation (see Table 3). We select non-lens objects for the negatives, which contains: 55 per cent galaxies that are randomly selected from the parent catalogue; 34 per cent spiral galaxies from Tadaki et al. (2020); 5 per cent stars from the SDSS spectroscopic star catalogue (Ahumada et al. 2020); 4 per cent galaxy groups or 'crowded' galaxies like LRG + egde-on galaxy (or arc-like feature); and 2 per cent dual point-like, tricky spiral or merger galaxies that are visually inspected from the parent catalogue (see the right panel in Fig. 1).

In order to identify blue sources, we select HSC gri-band images due to their excellent depth and quality. The FITS images in three bands are converted to RGB images scaled with an arcsinh stretch using HUMVI[4] (Marshall et al. 2016) and supplied to the CNN as vectors of 12 288 (64 × 64 × 3) floating-point numbers. To ensure that the colour-composite images contain no missing information regarding the colour of the sources/arcs, we explore the optimal configuration of contrast, colour balance, and brightness parameters when combining the three new images into an RGB colour composite. Before the CNN's training stage, we preprocess our data by normalizing each image brightness to be between 0 and 1.

[4]https://github.com/drphilmarshall/HumVI

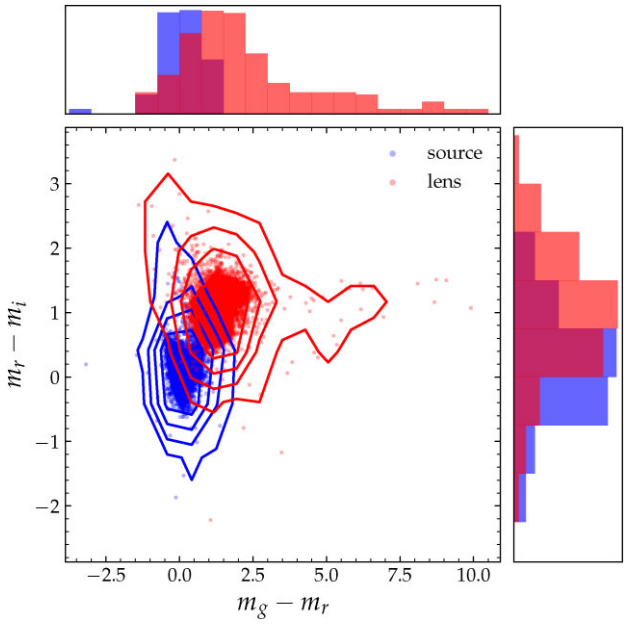

Figure 3. Distributions of colour–colour ($m_r - m_i$ versus $m_g - m_r$) diagram of the lens galaxies, and the sources.

Table 3. Details of training and test samples used in the analyses.

Training sample	Lenses	14 928
	Non-lenses	14 928
Validation sample	Lenses	3732
	Non-lenses	3732
Test sample	Lenses	220
	Non-lenses	78 665
	Composition of the non-lens sample	
Non-lenses used in training	Random Galaxies	55 per cent
	Spiral Galaxies	34 per cent
	Stars (SDSS Spectroscopic star)	5 per cent
	Groups or LRG + edge-on galaxies	4 per cent
	Doubles, 'tricky' spirals or mergers	2 per cent

Notes. See Section 4 for further details.

This normalization can help improve the network's performance and training efficiency by enhancing numerical stability, promoting faster convergence, aiding with generalization, preventing saturation of activation functions, and optimizing the training process. In general, data augmentation is a common practise in machine learning; it is used to expand the training set in order to prevent overfitting and teach the network rotational, translational and scaling invariance. Here, we use in-place data augmentation to make sure that, when the network is trained, it sees new variations of our data set at each and every epoch. This augmentation method is done at training time and not an 'additive' operation which is transforming the original data in the batch by a series of random transformation, then returning the randomly transformed into network for training. We investigate the optimal values for random values of the augmentation criteria while keeping the network architecture the same. We augment our data set applying the following transformations to the simulated and non-lens galaxy sample: (i) a random rotation in the range [–30 deg, 30 deg]; (ii) a random resizing by a factor in the range [0.8, 1.2]; (iii) a random flip along the horizontal axis; and (iv) and a random `channel_shift_range`[5]= 0.9.

Table 4. CNN architecture.

ID (1)	Type (2)	Size (3)	n (4)	Activation (5)	Param count (6)
1	Input	64 × 64	–	–	–
2	Convolutional	11 × 11	64	ReLU	23 296
3	Max pooling	2 × 2	–	–	–
4	Convolutional	7 × 7	128	ReLU	401 536
5	Dropout (0.2)	–	–	–	–
6	Convolutional	5 × 5	128	ReLU	409 728
7	Max pooling	2 × 2	–	–	–
8	Convolutional	5 × 5	256	ReLU	819 456
9	Dropout (0.2)	–	–	–	–
10	Convolutional	3 × 3	256	ReLU	590 080
11	Max pooling	2 × 2	–	–	–
12	Fully connected	1024	–	ReLU	2360 320
13	Dropout (0.2)	–	–	–	–
14	fully connected	1024	–	ReLU	1049 600
15	Dropout (0.2)	–	–	–	–
16	Fully connected	512	–	ReLU	524 800
17	Dropout (0.2)	–	–	–	–
18	Fully connected	512	–	ReLU	262 656
19	Fully connected	1	–	Sigmoid	513
Total params			6441 985		
Trainable params			6441 985		
Nontrainable params			0		

Notes. (1) ID of the layers. (2) Type of the layers. (3) Size of the data or the filters. (4) Number of the filters. (5) Activation function adopted in the layers. (6) Trainable parameters.

4.2 CNN architecture

The CNN architecture is inspired by LeNet (Lecun et al. 1998) and Jacobs et al. (2017), with modifications displayed in Table 4. The CNN consists of five convolutional layers followed by four fully connected hidden layers. Five dropout regularizations (Srivastava et al. 2014) are added to the network at intervals between layers to minimize the likelihood of overfitting by dropping 20 per cent of the output neurons at random during training with rectified linear unit (ReLU; Nair & Hinton 2010) non-linear activations. The output layer consists of a single neuron with sigmoid activation. Three Maxpooling layers with 2 × 2 kernel sizes and stride 2 are inserted between the convolutional layers to make the CNN invariant to local translations of the relevant features in *gri* image cutouts while reducing the network parameters. The network has a total of 6441 985 trainable parameters upon completion. In order to investigate the hyperparameters, we train different CNN architectures with random configurations over several cycles. We explore the models with 4–7 convolutional layers, different kernel sizes, 3–5 dropout layers, batchsizes ranging from 64 to 512, and dense units of 2–5. We also test the effect of different learning rates, in the range of 10^{-2}–10^{-5}, and dropout rates of 0.1–0.5. Our best network is summarized in Table 4.

We use the Adam optimization algorithm (Kingma & Ba 2014) to minimize the cross-entropy error function over the training data with a learning rate of 0.000 05. The CNN is trained for the maximum

[5]The `channel_shift_range` is used particularly to shift pixel values along an image's channels.

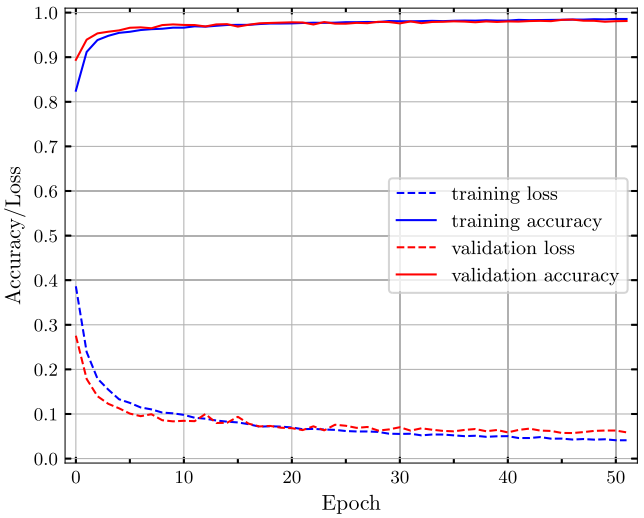

Figure 4. Accuracy (solid curves) and loss (dashed curves) as a function of training epoch. These metrics are obtained by evaluating the CNN on the training and validation data sets, which are then shown by the blue and red lines, respectively.

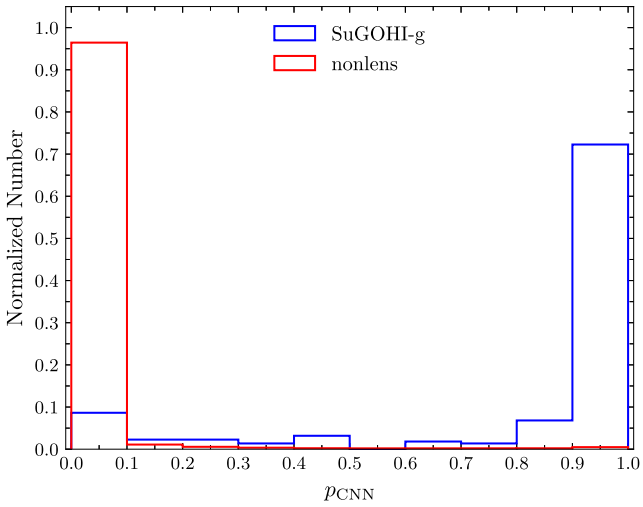

Figure 5. Histogram of the probabilities predicted by the trained CNN for all lens and non-lens of test sample.

allowed 100 epochs using mini-batch stochastic gradient descent with 128 images per batch. If the network does not provide improved accuracy or loss after five consecutive epochs, we terminate the training early. This network is implemented utilizing the PYTHON neural network library Keras (Chollet & others 2018) with the TensorFlow backend (Abadi et al. 2016). The CNN is trained on an NVIDIA RTX 3070 8GB. On average, network training requires less than an hour for a training data set like the one we used.

Completeness is measured on spectroscopically confirmed or grade A or B SuGOHI galaxy-scale lenses (Sonnenfeld et al. 2018; Wong et al. 2018; Sonnenfeld et al. 2020). We rejected a few lenses with large image separations $\gtrsim 3$ arcsec, indicating significant perturbation from the lens environment, as we have no intention of recovering such configurations. As test lenses, we use 220 SuGOHI-g lens systems. We collect the 78 665 non-lenses, including random galaxies from a parent catalogue; spiral galaxies from Tadaki et al. (2020); and stars from the SDSS spectroscopic star catalogue (Ahumada et al. 2020).

4.3 CNN performance

The CNN provides a score, $p_{\rm CNN}$, ranging from 0 to 1, with 1 for lenses and 0 for everything else (non-lenses). The evolution of the training loss for the network with optimized hyperparameters until epoch 52 (see Fig. 4) corresponds to the validation set's minimum binary cross-entropy loss without overfitting. The network achieved a training (validation) accuracy of 0.986 (0.981) and a loss of 0.041 (0.059). The small difference between the two curves (generalization gap) indicates that the model's predictions on new data with similar properties to the training set are relatively stable. Using the test set, the final network performance was characterized. In Fig. 5, we show the probabilities predicted by the model for all lens and non-lens test examples. When $p_{\rm CNN} > 0.9$, the distribution is dominated by lenses.

To evaluate the number of lenses correctly identified, we use a receiver operating characteristic (ROC) curve which compares the true positive rate (TPR) to the false positive rate (FPR) as functions of the decision threshold applied to the score and precision–recall (PR) curves for the trained CNN showing the precision as function of the recall or TPR. We use the following definitions of TPR or recall, FPR, and precision:

$$\mathrm{TPR} = \frac{\mathrm{TP}}{\mathrm{TP}+\mathrm{FN}}; \mathrm{FPR} = \frac{\mathrm{FP}}{\mathrm{FP}+\mathrm{TN}}; \mathrm{precision} = \frac{\mathrm{TP}}{\mathrm{TP}+\mathrm{FP}}, \quad (3)$$

where TP, FP, TN, and FN are true positive, false positive, true negative, and false negative, respectively. In general, the excellent performance are shown by the ROC and PR curves in Fig. 6. The ROC curve illustrates the performance of a binary classifier in distinguishing between the two classes as the decision threshold is altered. The Area Under the ROC Curve (AUC) of our CNN are 0.976 and 0.971, for imbalanced (0.3–99.7) and balanced (50–50) test sample, respectively. For balanced test sample, the PR curve shows that the network can classify all objects as lens sample would yield a precision (purity) of 97.3 per cent at a recall (completeness) of 82.3 per cent of SuGOHI-g lenses in the test set with an FPR of 1.3 per cent for $p_{\rm CNN} = 0.5$ as the threshold; and a precision of 98.8 per cent at a recall of 72.3 per cent of SuGOHI-g lenses with an FPR of 0.49 per cent for $p_{\rm CNN} = 0.9$ as a threshold (see Table 5). We find that the misclassified test lenses (see Fig. 7) contain compact or fainter lens galaxies, lensed sources with redder colours, stronger blending with lens light or companion galaxies, or lower source-to-lens flux ratios, or lensed by group/cluster. Our simulations include fewer examples of each of these configurations.

4.4 Visual inspection

We applied the trained CNN to the *gri* cutouts of all 2.4 million galaxies in order to determine their score $p_{\rm CNN}$. The CNN identifies 55 469, 20 241, and 1830 as candidate lenses with $p_{\rm CNN} > 0.5$, $p_{\rm CNN} > 0.9$, and $p_{\rm CNN} = 1.0$, respectively. About 0.86 per cent of the parent sample has $p_{\rm CNN} > 0.9$. We note that several candidates have a blue feature close to a red galaxy with a very faint or no counter blue image. This is possibly due to our training data set being sensitive to small Einstein radii. After an initial visual inspection performed by a single inspector (ATJ) to remove definite non-lenses, a 'good' sample of 1522 potential lens candidates is determined.

We inspect RGB images of these candidates using custom written, java-based application called VISAPP (More et al. 2016), which displays PNG images made with *gri* imaging. VISAPP utilizes capabilities of the invert, zoom, contrast, and brightness adjustment

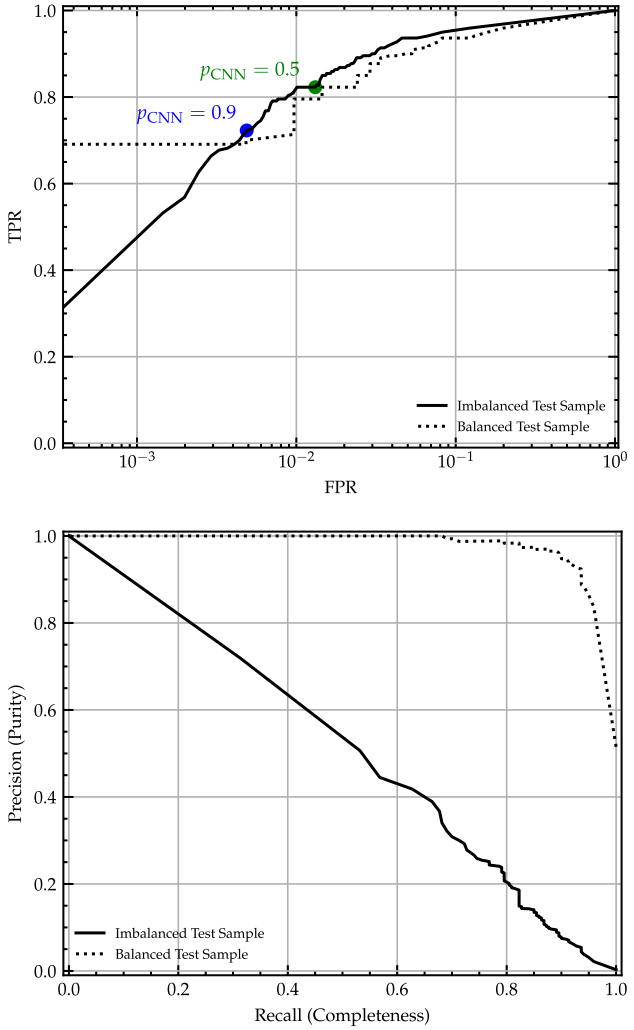

Figure 6. Top panel**:** receiver operating characteristic curves for the trained CNN showing the true position rate (TPR) as function of the false positive rate (FPR) for different lens identification thresholds. The corresponding area under curve (AUC) are 0.976 and 0.971, for imbalanced and balanced test sample, respectively. Bottom panel**:** PR curves for the trained CNN showing the precision as function of the recall. Note that this performances describes a test data set with a 50–50 split (for balanced) and a 0.3–99.7 split (for imbalanced) between lens and non-lens containing images. Number of test sample is shown in Table 5.

features, as well as the remark area. Fig. 8 shows a snapshot of the classification interface from the VISAPP with an inverted and zoomed image. We assign each candidate a grade between 0 and 3, using the grading convention from Sonnenfeld et al. (2020), where 0 means 'almost certainly not a lens', 1 means 'possibly a lens', 2 means 'probably a lens', and 3 means 'almost certainly a lens'. There are comment columns for the candidates that require further discussion. It is possible to invert the images's colour, zoom in or out and shift it. The grades used throughout the paper are the mean grade, $\langle Gr \rangle$, assigned by authors ATJ, AM, KTI, DCYC, KCW, and PWP.

Next, we implemented the scheme outlined below (Sonnenfeld et al. 2018):

(i) A: $\langle Gr \rangle > 2.5$,
(ii) B: $1.5 < \langle Gr \rangle \leq 2.5$,
(iii) C: $0.5 < \langle Gr \rangle \leq 1.5$, and
(iv) Not a lens: $\langle Gr \rangle \leq 0.5$.

Table 5. Results of the lens search on the parent catalogue.

Criteria	Number
Image tested	2350 061
First candidates set	
$p_{CNN} > 0.5$	55 469
$p_{CNN} > 0.9$	20 241
$p_{CNN} = 1.0$	1830
Second candidates set	1522
Final candidates set	1292
Grade A	43
Grade B	269
Known (A or B)	215
New (A or B)	97
Grade C	880
Known (C)	289
For balanced test sample (50–50)	
Precision (purity)	
($p_{CNN} > 0.5$)	97.3 per cent
($p_{CNN} > 0.9$)	98.8 per cent
Recall (completeness)	
($p_{CNN} > 0.5$)	82.3 per cent
($p_{CNN} > 0.9$)	72.3 per cent
For imbalanced test sample (0.3–99.7)	
Precision (purity)	
($p_{CNN} > 0.5$)	14.9 per cent
($p_{CNN} > 0.9$)	29.3 per cent
Recall (completeness)	
($p_{CNN} > 0.5$)	82.3 per cent
($p_{CNN} > 0.9$)	72.3 per cent
The fraction of grades A and B with $\langle Gr \rangle > 1.5$	
$0.95 < p_{CNN} \leq 1.00$	268/312
$0.90 < p_{CNN} \leq 0.95$	44/312

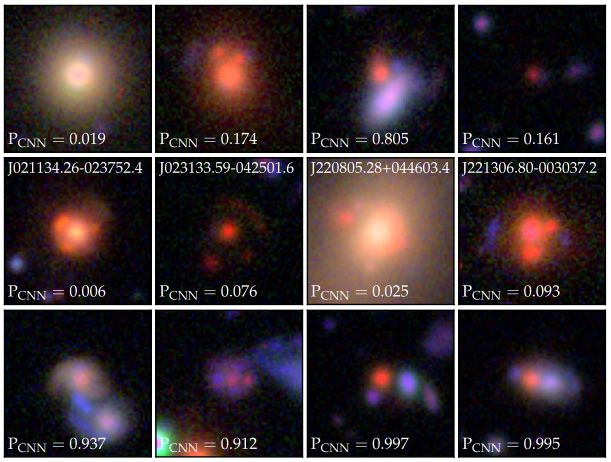

Figure 7. Example of colour composite images of test data sets that the CNN missed or misclassified. Top row: simulated test lenses with $P_{CNN} < 0.9$. Second row: SuGOHI galaxy-scale with $P_{CNN} < 0.9$. Third row: non-lenses which show dust lanes, arcs, or blue dots appear around LRGs with $P_{CNN} > 0.9$.

Then, the grades were compiled and averaged, and each grader's scores were revealed and compared. Graders were then allowed to adjust their scores, particularly for contentious objects with disparate scores or scores close to the grade thresholds, which were probably due to personal grading experience or human fatigue. During this

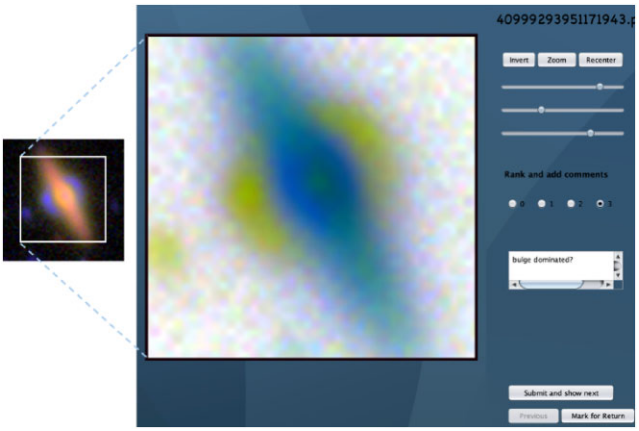

Figure 8. Left panel: example colour image of a lens system with a size of 10.752 arcsec on the side. Blue right panel: snapshot of the classification interface of the VISAPP showing the same lens system in a colour-inverted and zoomed mode.

stage, we also used the HSC PDR2 map[6] for additional inspection, if necessary.

5 RESULTS

In total, we discover 43 grade A, 269 grade B, and 880 grade C candidates. The results are summarized in Table 5, which include the number of parent sample, lens candidates, purity, and completeness. The full list of the grade A and some examples of grade B candidates are given in Table 6. We note that the nearby lensed arcs could affect the i-band magnitude and photometric redshift. We show colour composite images of the grade A candidates in Fig. 9 and of the grade B candidates in Fig. A1. The lens redshift distribution of the grade A and grade B candidates is shown in Fig. 10 with the peak at $z_{\ell,\ \mathrm{phot}} \sim 0.7$ and $z_{\ell,\ \mathrm{spec}} \sim 0.6$. While some lens candidates which were grade C from previous SuGOHI publications have been upgraded to a higher grade in recent references, we list the grade C lens candidates in the Appendix. The fraction of grades A and B with $\langle Gr \rangle > 1.5$ among CNN recommendations, decreases rapidly when lowering the threshold p_{CNN}. We estimate that 85.9 per cent of the highest scores $0.95 < p_{\mathrm{CNN}} \leq 1.00$ which has $\langle Gr \rangle > 1.5$, and about 14.1 per cent for $0.90 < p_{\mathrm{CNN}} \leq 0.95$. After final visual inspection, taking $\langle Gr \rangle > 0.5$ to be TP and $\langle Gr \rangle \leq 0.5$ to be FP, the purity is 78.32 per cent. In general, we find that the majority of lensed sources have a blue colour, which is due to the selection effect from our training sample.

Separately from this work, Cañameras et al. (2021) and Shu et al. (2022) have recently applied machine-learning-based lens search algorithms to the HSC-SSP PDR2 (Aihara et al. 2019) and have published lens candidates from these searches. Our parent sample and training set have smaller number of galaxies compared to Cañameras et al. (2021) and Shu et al. (2022), however, we still are able to discover a comparable number of lenses (see details in More et al. 2024). We note that about 51 per cent of our parent sample and the parent sample from Cañameras et al. (2021) overlap. There is some overlap in the candidates we discovered as we used the HSC-SSP data set. Recently, More et al. (2024) presented a systematic comparison of neural network performance that included results from Cañameras et al. (2021), Shu et al. (2022), this work, and Ishida et al., in preparation. They provided an analysis of

[6]https://hsc-release.mtk.nao.ac.jp/hscMap-pdr2/app/#/

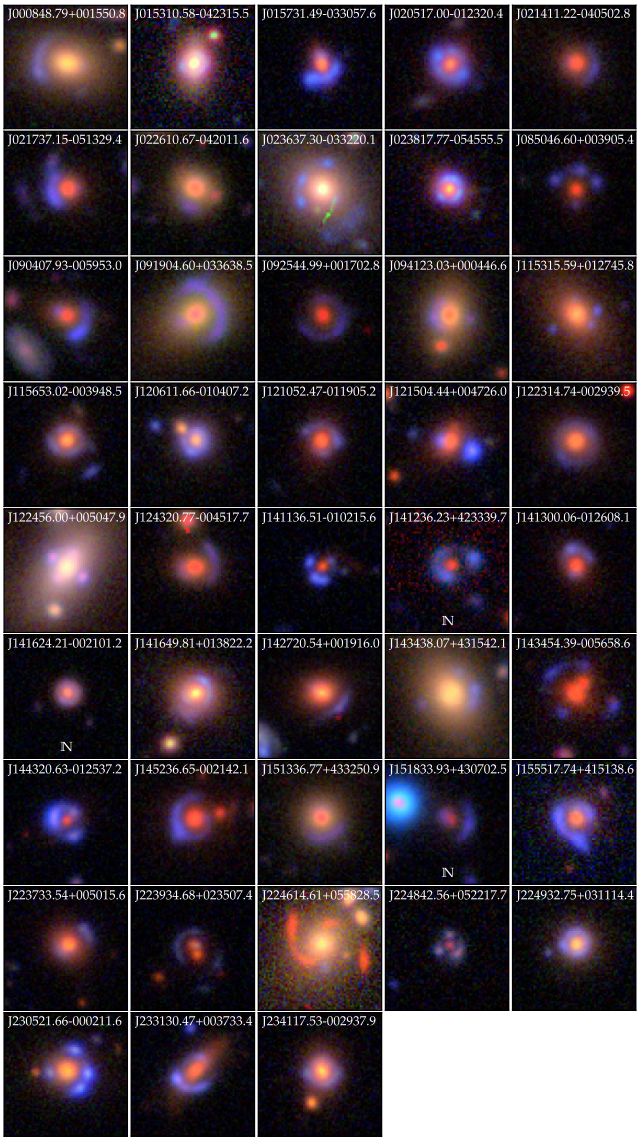

Figure 9. Images for the 43 lens candidates with grades A. All images are oriented with North up and East to the left. ℕ letters indicate newly discovered candidates.

several neural networks with different training data sets and/or parent catalogues, and evaluated the networks' performance on common test samples, performance when trained on interchanged data sets, and performance on SuGOHI lenses. Figs 1–3, as well as section 5.3 of More et al. (2024), show full examples of lens systems that were missed in this work but retrieved by others. Fig. 11 shows a subset of confirmed lenses and lens candidates from the common test samples in More et al. (2024). Previous studies by Cañameras et al. (2021) and Shu et al. (2022) have successfully classified some lens systems, denoted by C21 and S22 on the top of each cutout in Fig. 11. Some lens systems are still not classified by all networks, which suggests that we should improve and investigate hyperparameters in the training data sets.

We have identified and cross-matched previous candidates with our candidates and listed the relevant references in Table 6. We find 504 overlapping candidates with 215 and 289 candidates from grade A or B, and grade C, respectively. We find that 143 of 289 overlapping grade C have a higher grade in previous searches. There are 207

Table 6. The grade A and B strong lens candidates.

HSC_ID	α(J2000)	δ(J2000)	$m_{i,\ell}$	$z_{\ell,\mathrm{phot}}$	$z_{\ell,\mathrm{spec}}$	$\mathrm{P_{CNN}}$	$\langle Gr \rangle$	References
J000848.79+001550.8	2.203 33	0.264 12	19.57	0.348	0.397	0.901	2.667	e, l, t
J015310.58–042315.5	28.294 12	−4.387 66	19.01	0.306	–	0.990	2.667	t
J015731.49–033057.6	29.381 25	−3.516 03	17.83	0.683	0.621	1.000	2.667	a, l, t
J020517.00–012320.4	31.320 86	−1.389 01	19.57	0.770	–	0.997	2.667	l, m
J021411.22–040502.8	33.546 76	−4.084 11	17.99	0.662	0.609	0.987	2.667	b, e, g, l, n, p, t
J021737.15–051329.4	34.404 81	−5.224 86	17.96	0.629	0.646	0.996	3.000	c, e, m, n, p, t
J022610.67–042011.6	36.544 47	−4.336 58	18.57	0.469	0.495	0.991	2.667	a, c
J023637.30–033220.1	39.155 45	−3.538 93	20.03	0.275	0.269	1.000	3.000	a, e, l, t
J023817.77–054555.5	39.574 04	−5.765 43	20.13	0.594	0.599	0.999	3.000	a, c, d, l
J085046.60+003905.4	132.694 20	0.651 50	20.98	0.951	–	0.988	3.000	f, l, t
J090407.93–005953.0	136.033 06	−0.998 07	18.77	0.622	–	1.000	3.000	g, l, n, t
J091904.60+033638.5	139.769 17	3.610 72	20.28	0.406	0.444	0.963	2.833	a, e, k, l, t
J092544.99+001702.8	141.437 48	0.284 13	20.42	0.840	–	0.908	3.000	e, f, l, t
J094123.03+000446.6	145.345 96	0.079 64	21.28	0.456	0.486	1.000	2.667	b, l, t
J115315.59+012745.8	178.31498	1.462 74	20.09	0.504	–	1.000	2.833	e, f, t
J115653.02–003948.5	179.220 93	−0.663 50	21.31	0.540	0.508	0.991	2.667	a, i, t
J120611.66–010407.2	181.548 61	−1.068 67	18.18	0.534	–	0.997	2.833	l, t
J121052.47–011905.2	182.718 66	−1.318 14	21.26	0.683	0.700	0.998	2.667	a, c, d, l, t
J121504.44+004726.0	183.768 50	0.790 57	20.32	0.655	0.642	1.000	2.667	c, r
J122314.74–002939.5	185.811 43	−0.494 32	18.26	0.541	0.547	0.990	2.667	b, l, t
J122456.00+005047.9	186.233 36	0.846 65	17.98	0.226	–	0.996	2.667	l, q
J124320.77–004517.7	190.836 55	−0.754 94	18.23	0.634	0.654	0.938	2.667	b, i, l, t
J141136.51–010215.6	212.902 14	−1.037 69	20.96	0.993	0.949	1.000	3.000	d, f
J141236.23+423339.7	213.150 97	42.561 05	20.01	0.854	–	0.996	2.667	This Work
J141300.06–012608.1	213.250 27	−1.435 61	20.81	0.757	0.749	0.999	2.667	a, c, d, l
J141624.21–002101.2	214.100 91	−0.350 36	20.18	0.631	–	0.981	2.667	This work
J141649.81+013822.2	214.207 56	1.639 51	20.02	0.313	–	1.000	2.667	f, i, l, t
J142720.54+001916.0	216.835 60	0.321 11	17.32	0.558	0.551	0.981	2.833	a, c, l, t
J143438.07+431542.1	218.658 64	43.261 71	20.04	0.342	0.385	0.998	2.833	e, l, t
J143454.39–005658.6	218.726 64	−0.949 64	18.36	0.729	0.728	0.948	2.667	a, e, t
J144320.63–012537.2	220.835 98	−1.427 00	18.83	0.952	0.890	0.983	2.667	d, f
J145236.65–002142.1	223.152 72	−0.361 71	18.15	0.695	0.733	0.997	2.667	a, l, t
J151336.77+433250.9	228.403 22	43.547 50	20.85	0.469	0.487	0.968	2.667	b, l, t
J151833.93+430702.5	229.641 40	43.117 39	19.90	0.986	–	0.941	2.667	This work
J155517.74+415138.6	238.823 92	41.860 74	20.34	0.600	0.555	1.000	2.667	a, k, l, t
J223733.54+005015.6	339.389 76	0.837 67	19.97	0.634	0.605	0.986	2.667	a, c, t
J223934.68+023507.4	339.894 53	2.585 40	17.41	0.981	–	0.961	2.667	e, f, t
J224614.61+055828.5	341.560 90	5.974 59	20.00	0.274	0.340	0.957	3.000	e, l, t
J224842.56+052217.7	342.177 37	5.371 59	20.21	0.904	–	0.920	2.667	t
J224932.75+031114.4	342.386 47	3.187 36	20.36	0.315	–	0.998	3.000	l, t
J230521.66–000211.6	346.340 29	−0.036 58	20.27	0.497	0.492	1.000	3.000	b, l, m, t
J233130.47+003733.4	352.877 00	0.625 95	20.11	0.535	0.552	1.000	2.833	b, l, m, t
J234117.53–002937.9	355.32304	−0.493 88	18.99	0.511	0.531	0.979	2.833	l, t, u
J000326.35–002140.8	0.859 80	−0.361 33	18.34	0.794	–	1.000	1.667	This work
J001313.60+002759.9	3.306 68	0.466 65	18.95	0.542	–	0.990	1.667	t
J011219.08–001539.3	18.079 51	−0.260 94	20.63	0.541	–	0.985	1.667	This work
J011225.76–002247.0	18.107 37	−0.379 74	21.50	0.476	0.466	0.990	2.167	e
J012204.59–002222.1	20.519 15	−0.372 82	20.78	1.036	0.848	0.989	1.667	This work
J012402.54–004559.3	21.010 60	−0.766 48	20.02	0.537	0.543	0.964	1.667	t
J015702.39–053436.0	29.259 98	−5.576 69	19.39	0.319	–	0.936	2.500	This work
J015713.94–045446.9	29.308 09	−4.913 04	21.41	0.774	–	0.993	1.833	This work
J020832.14–043315.8	32.133 93	−4.554 39	19.30	0.761	–	0.988	2.000	e, h, l, t
J095906.48+024524.8	149.777 04	2.756 91	19.37	0.317	0.346	0.954	1.833	o
J115944.63–000728.2	179.936 00	−0.124 52	20.92	0.734	0.332	0.988	2.333	r
J232557.38–005226.8	351.489 09	−0.874 12	20.11	0.794	–	0.980	2.167	j, l, m
J234248.68–012032.6	355.702 84	−1.342 39	18.00	0.578	0.527	0.998	2.000	l, s
⋮	⋮	⋮	⋮	⋮	⋮	⋮	⋮	⋮

Notes. Column 1 is ID of the system name. Columns 2 and 3 are right ascension and declination of the lens galaxy, respectively. Columns 4 and 5 are the *i*-band CModel magnitude and photometric redshift of the lens galaxy provided by the HSC catalogue, respectively. Columns 6 gives the spectroscopic redshifts of the lens galaxy inferred from SDSS DR16. Column 7 is the CNN score. Column 8 is the average visual-inspection score of the lens system.'This Work' indicates a completely new discovery. Other relevant references in Column 9 are (a) Sonnenfeld et al. (2018), (b) Wong et al. (2018), (c) Sonnenfeld et al. (2019), (d) Chan et al. (2020), (e) Jaelani et al. (2020b), (f) Sonnenfeld et al. (2020), (g) More et al. (2012), (h) More et al. (2016), (i) Petrillo et al. (2019), (j) Huang et al. (2020), (k) Cañameras et al. (2020), (l) Cañameras et al. (2021), (m) Jacobs et al. (2019), (n) Cabanac et al. (2007), (o) Faure et al. (2008), (p) Gavazzi et al. (2014), (q) Li et al. (2020), (r) Brownstein et al. (2012), (s) Shu et al. (2016), (t) Shu et al. (2022), and (u) Wong et al. (2022). The full list is available at the http://www-utap.phys.s.u-tokyo.ac.jp/ oguri/sugohi/.

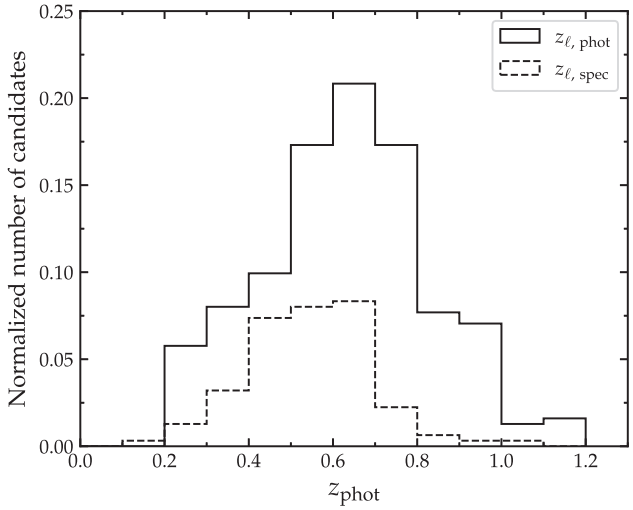

Figure 10. Histogram of lens (photometric) redshifts of the grade A and grade B candidates found in this work. Spectroscopic redshifts available only for a subsample.

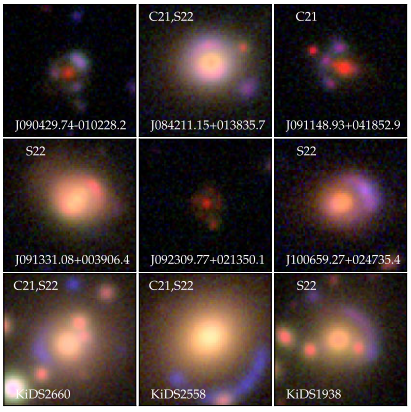

Figure 11. A subset of grade A and B confirmed lenses and lens candidates from the common test samples in More et al. (2024). The neural networks that successfully classify these cutouts as lenses are listed at the top left.

and 160 candidates from all grades that overlap with the findings from Cañameras et al. (2021) and Shu et al. (2022), respectively. Our CNN also recovers 32 group- and cluster-scale lens candidates, although it is not optimized for these systems. Many candidates with a blue arc feature near a red galaxy have a lower grade, as seen in Table B1. Rojas et al. (2023) found that is difficult for experts to recover candidates with Einstein radius less than 1.2 times the seeing during visual inspection.

6 SUMMARY

We present new candidates for galaxy-scale strong gravitational lenses from the HSC-SSP PDR2, covering 800 deg^2 in the *gri* bands, using a CNN as part of the SuGOHI project. In order to identify possible galaxy-scale lenses, we use strict pre-selection criteria, such as multiband magnitudes, stellar mass, star formation rate, extendedness limit, and photometric redshift range, resulting in about 2.4 million galaxies of parent sample. By initially adopting a conventional threshold, $p_{\mathrm{CNN}} > 0.9$, we find 20 241 candidates which are then refined to 1522 systems with lensing features for further inspection.

On the basis of visual inspections of the cutouts, six authors independently graded the strong lens candidates. According to the average visual inspection scores, 312 candidates identified by the CNN are considered grade A or B (i.e. definite or probable), and 880 are grade C (possible) strong-lens candidates. This list was cross-referenced with our extensive compilation of strong gravitational lenses previously published as confirmed systems or candidates in order to identify duplicates. Among the candidates, there are 97 new discoveries (3 from grade A and 94 from grade B, respectively). We find that 143 grade C candidates were graded as A or B in previous literature. The (photometric) redshift of the candidate lens galaxies range from 0.2 to 1.2. Follow-up spectroscopy will confirm these lenses and measure source redshifts so that detailed lens modelling can yield scientific results.

ACKNOWLEDGEMENTS

We are also grateful to Honoka Murakami and Sherry H. Suyu for their valuable contributions and fruitful discussions, which have significantly improved the quality of this manuscript. We also thank the anonymous referee for useful comments on the paper. This research is supported by Program Riset Unggulan Pusat dan Pusat Penelitian (RU3P) 2023 which is funded by Direktorat Penerapan Ilmu dan Teknologi Multidisiplin (DPITM) Insitut Teknologi Bandung. This work also is supported Japan Society for the Promotion of Science (JSPS) KAKENHI Grant Number JP20K14511. RC thanks the Max Planck Society for support through the Max Planck Research Group for S.H.S. This project has received funding from the European Research Council (ERC) under the European Union's Horizon 2020 research and innovation programme (LENSNOVA: grant agreement No 771776).

The Hyper Suprime-Cam (HSC) collaboration includes the astronomical communities of Japan and Taiwan, and Princeton University. The HSC instrumentation and software were developed by the National Astronomical Observatory of Japan (NAOJ), the Kavli Institute for the Physics and Mathematics of the Universe (Kavli IPMU), the University of Tokyo, the High Energy Accelerator Research Organization (KEK), the Academia Sinica Institute for Astronomy and Astrophysics in Taiwan (ASIAA), and Princeton University. Funding was contributed by the FIRST program from the Japanese Cabinet Office, the Ministry of Education, Culture, Sports, Science and Technology (MEXT), the Japan Society for the Promotion of Science (JSPS), Japan Science and Technology Agency (JST), the Toray Science Foundation, NAOJ, Kavli IPMU, KEK, ASIAA, and Princeton University.

This paper is based on data collected at the Subaru Telescope and retrieved from the HSC data archive system, which is operated by Subaru Telescope and Astronomy Data Center (ADC) at NAOJ. Data analysis was in part carried out with the cooperation of Center for Computational Astrophysics (CfCA) at NAOJ. We are honored and grateful for the opportunity of observing the Universe from Maunakea, which has the cultural, historical and natural significance in Hawaii. This paper makes use of software developed for Vera C. Rubin Observatory. We thank the Rubin Observatory for making their code available as free software at http://pipelines.lsst.io/. Funding for SDSS-III has been provided by the Alfred P. Sloan Foundation, the Participating Institutions, the National Science Foundation, and the U.S. Department of Energy Office of Science. The SDSS-III web site is http://www.sdss3.org/. SDSS-III is managed by the Astrophysical Research Consortium for the Participating Institutions of the SDSS-III Collaboration including the University of Arizona, the Brazilian Participation Group, Brookhaven National Laboratory, Carnegie Mellon University, University of Florida, the

French Participation Group, the German Participation Group, Harvard University, the Instituto de Astrofisica de Canarias, the Michigan State/Notre Dame/JINA Participation Group, Johns Hopkins University, Lawrence Berkeley National Laboratory, Max Planck Institute for Astrophysics, Max Planck Institute for Extraterrestrial Physics, New Mexico State University, New York University, Ohio State University, Pennsylvania State University, University of Portsmouth, Princeton University, the Spanish Participation Group, University of Tokyo, University of Utah, Vanderbilt University, University of Virginia, University of Washington, and Yale University.

This research made use of Astropy[7] (Astropy Collaboration et al. 2013, 2018), NUMPY (Harris et al. 2016), MATPLOTLIB (Caswell et al. 2019), SIMCT (More et al. 2016), and TENSORFLOW (Developers 2022).

DATA AVAILABILITY

The basic information of the lens candidates can be browsed or downloaded from the SuGOHI online database http://www-utap.phys.s.u-tokyo.ac.jp/~oguri/sugohi/ and imaging data from the HSC-SSP Public Data Release 2 https://hsc-release.mtk.nao.ac.jp/doc/. The lens and non-lens test data sets are available upon reasonable request to the authors.

REFERENCES

Abadi M. et al., 2016, preprint (arXiv:1603.04467)
Ahumada R. et al., 2020, ApJS, 249, 3
Aihara H. et al., 2019, PASJ, 71, 114
Allingham J. F. V. et al., 2023, MNRAS, 522, 1118
Astropy Collaboration 2013, A&A, 558, A33
Astropy Collaboration 2018, AJ, 156, 123
Auger M. W., Treu T., Bolton A. S., Gavazzi R., Koopmans L. V. E., Marshall P. J., Moustakas L. A., Burles S., 2010, ApJ, 724, 511
Bernardi M. et al., 2003, AJ, 125, 1866
Birrer S. et al., 2020, A&A, 643, A165
Bosch J. et al., 2018, PASJ, 70, S5
Brownstein J. R. et al., 2012, ApJ, 744, 41
Cañameras R. et al., 2020, A&A, 644, A163
Cañameras R. et al., 2021, A&A, 653, L6
Cabanac R. A. et al., 2007, A&A, 461, 813
Caswell T. A. et al., 2019, matplotlib/matplotlib v3.1.0. Zenodo
Chan J. H. H., Suyu S. H., Chiueh T., More A., Marshall P. J., Coupon J., Oguri M., Price P., 2015, ApJ, 807, 138
Chan J. H. H. et al., 2020, A&A, 636, A87
Chan J. H. H. et al., 2023, MNRAS, 527, 6253
Chollet F., others, 2018, Astrophysics Source Code Library, record ascl:1806.022
Coupon J., Czakon N., Bosch J., Komiyama Y., Medezinski E., Miyazaki S., Oguri M., 2018, PASJ, 70, S7
Developers T., 2022, TensorFlow. Zenodo
Erben T. et al., 2013, MNRAS, 433, 2545
Faure C. et al., 2008, ApJS, 176, 19
Faure C. et al., 2009, ApJ, 695, 1233
Furusawa H. et al., 2018, PASJ, 70, S3
Gavazzi R., Marshall P. J., Treu T., Sonnenfeld A., 2014, ApJ, 785, 144
Gilman D., Birrer S., Nierenberg A., Treu T., Du X., Benson A., 2020, MNRAS, 491, 6077
Harris D. W. et al., 2016, AJ, 151, 155
Hezaveh Y. D. et al., 2016, ApJ, 823, 37
Hildebrandt H. et al., 2012, MNRAS, 421, 2355
Hsueh J. W., Enzi W., Vegetti S., Auger M. W., Fassnacht C. D., Despali G., Koopmans L. V. E., McKean J. P., 2020, MNRAS, 492, 3047
Huang S. et al., 2018, PASJ, 70, S6
Huang X. et al., 2020, ApJ, 894, 78
Huang X. et al., 2021, ApJ, 909, 27
Inoue K. T., Minezaki T., Matsushita S., Chiba M., 2016, MNRAS, 457, 2936
Inoue K. T., Minezaki T., Matsushita S., Nakanishi K., 2023, ApJ, 954, 197
Jacobs C., Glazebrook K., Collett T., More A., McCarthy C., 2017, MNRAS, 471, 167
Jacobs C. et al., 2019, ApJS, 243, 17
Jaelani A. T. et al., 2020a, MNRAS, 494, 3156
Jaelani A. T. et al., 2020b, MNRAS, 495, 1291
Jaelani A. T. et al., 2021, MNRAS, 502, 1487
Jauzac M., Klein B., Kneib J.-P., Richard J., Rexroth M., Schäfer C., Verdier A., 2021, MNRAS, 508, 1206
Kawanomoto S. et al., 2018, PASJ, 70, 66
Keeton C. R., 2001, preprint(astro-ph/0102340)
Kingma D. P., Ba J., 2014, preprint (arXiv:1412.6980)
Komiyama Y. et al., 2018, PASJ, 70, S2
Koopmans L. V. E., Treu T., Bolton A. S., Burles S., Moustakas L. A., 2006, ApJ, 649, 599
Kormann R., Schneider P., Bartelmann M., 1994, A&A, 284, 285
Lecun Y., Bottou L., Bengio Y., Haffner P., 1998, Proc. IEEE, 86, 2278
Li R. et al., 2020, ApJ, 899, 30
Li R. et al., 2021, ApJ, 923, 16
Limousin M. et al., 2009, A&A, 502, 445
Marques-Chaves R. et al., 2017, ApJ, 834, L18
Marshall P. J. et al., 2016, MNRAS, 455, 1171
Metcalf R. B. et al., 2019, A&A, 625, A119
Miyazaki S. et al., 2018, PASJ, 70, S1
More A., Cabanac R., More S., Alard C., Limousin M., Kneib J. P., Gavazzi R., Motta V., 2012, ApJ, 749, 38
More A. et al., 2016, MNRAS, 455, 1191
More A. et al., 2017, MNRAS, 465, 2411
More A. et al., 2024, MNRAS, 533, 525
Nair V., Hinton G. E., 2010, in ICML
Newman A. B., Treu T., Ellis R. S., Sand D. J., 2013, ApJ, 765, 25
Nierenberg A. M. et al., 2017, MNRAS, 471, 2224
Oguri M., Bayliss M. B., Dahle H., Sharon K., Gladders M. D., Natarajan P., Hennawi J. F., Koester B. P., 2012, MNRAS, 420, 3213
Parker L. C., Hudson M. J., Carlberg R. G., Hoekstra H., 2005, ApJ, 634, 806
Petrillo C. E. et al., 2019, MNRAS, 484, 3879
Refsdal S., 1964, MNRAS, 128, 307
Rojas K. et al., 2023, MNRAS, 523, 4413
Shajib A. J., Treu T., Birrer S., Sonnenfeld A., 2021, MNRAS, 503, 2380
Shu Y. et al., 2016, ApJ, 824, 86
Shu Y., Cañameras R., Schuldt S., Suyu S. H., Taubenberger S., Inoue K. T., Jaelani A. T., 2022, A&A, 662, A4
Sonnenfeld A., Treu T., Marshall P. J., Suyu S. H., Gavazzi R., Auger M. W., Nipoti C., 2015, ApJ, 800, 94
Sonnenfeld A. et al., 2018, PASJ, 70, S29
Sonnenfeld A., Jaelani A. T., Chan J., More A., Suyu S. H., Wong K. C., Oguri M., Lee C.-H., 2019, A&A, 630, A71
Sonnenfeld A. et al., 2020, A&A, 642, A148
Srivastava N., Hinton G., Krizhevsky A., Sutskever I., Salakhutdinov R., 2014, J. Mach. Learn. Res., 15, 1929
Tadaki K.-i., Iye M., Fukumoto H., Hayashi M., Rusu C. E., Shimakawa R., Tosaki T., 2020, MNRAS, 496, 4276
Tanaka M., 2015, ApJ, 801, 20
Tanaka M. et al., 2018, PASJ, 70, S9
Vegetti S., Koopmans L. V. E., Bolton A., Treu T., Gavazzi R., 2010, MNRAS, 408, 1969
Vegetti S., Lagattuta D. J., McKean J. P., Auger M. W., Fassnacht C. D., Koopmans L. V. E., 2012, Nature, 481, 341
Wong K. C. et al., 2018, ApJ, 867, 107
Wong K. C. et al., 2020, MNRAS, 498, 1420
Wong K. C., Chan J. H. H., Chao D. C. Y., Jaelani A. T., Kayo I., Lee C.-H., More A., Oguri M., 2022, PASJ, 74, 1209
Zaborowski E. A. et al., 2023, ApJ, 954, 68

[7] http://www.astropy.org

APPENDIX A: IMAGES OF 269 GRADE B CANDIDATE

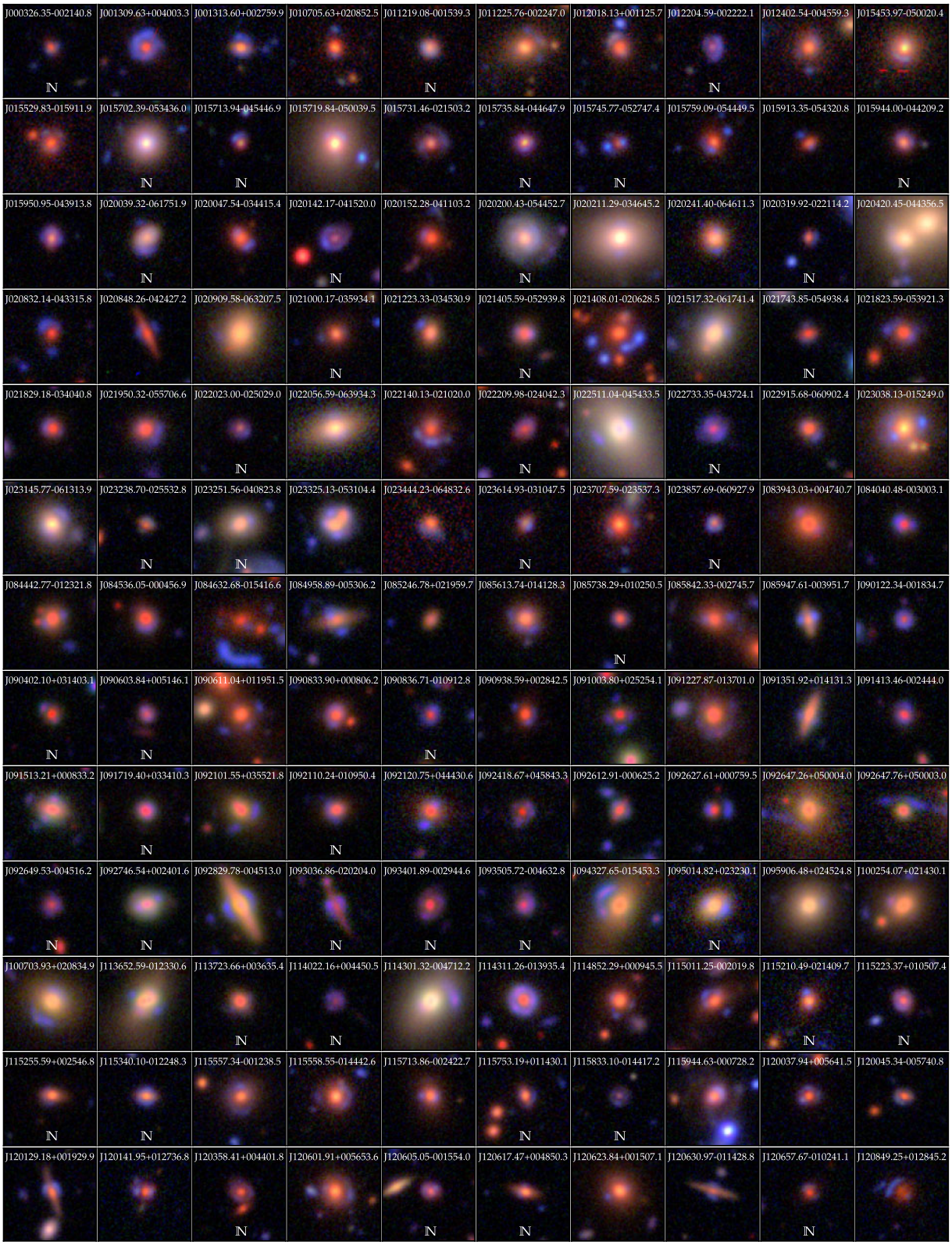

Figure A1. Images for the 269 lens candidates with grades B. All images are oriented with North up and East to the left. ℕ letters indicate the new ones.

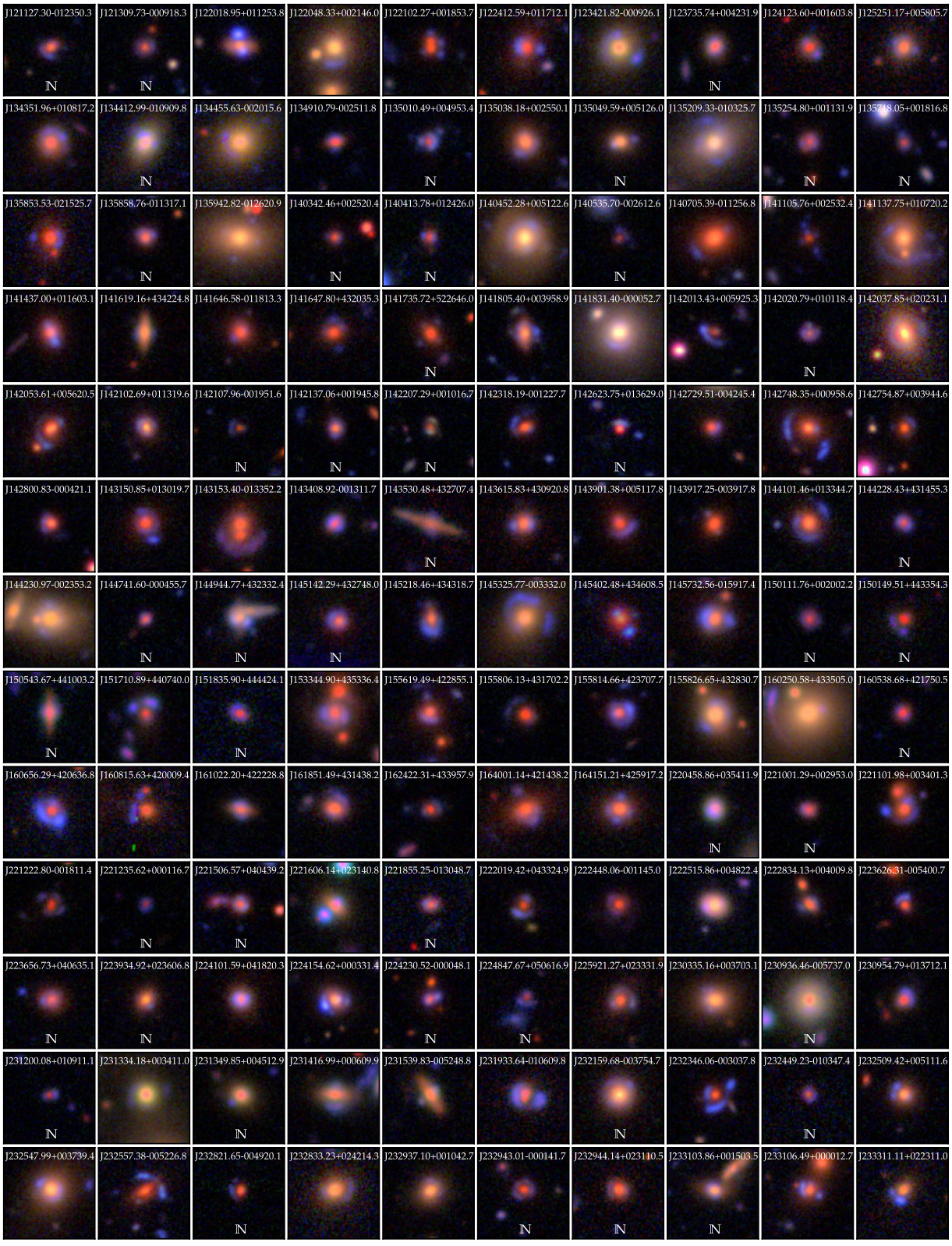

Figure A1. (*Continued.*)

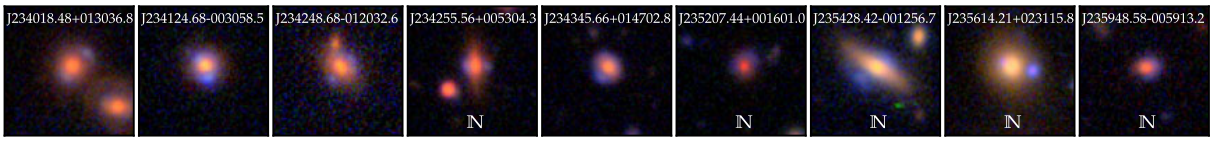

Figure A1. (*Continued.*)

APPENDIX B: IMAGES OF 143 GRADE C CANDIDATE

The full list of 880 grade C is also available at http://www-utap.phys.s.u-tokyo.ac.jp/ oguri/sugohi/. Here, we show 143 grade C candidates which had higher grade in previous references.

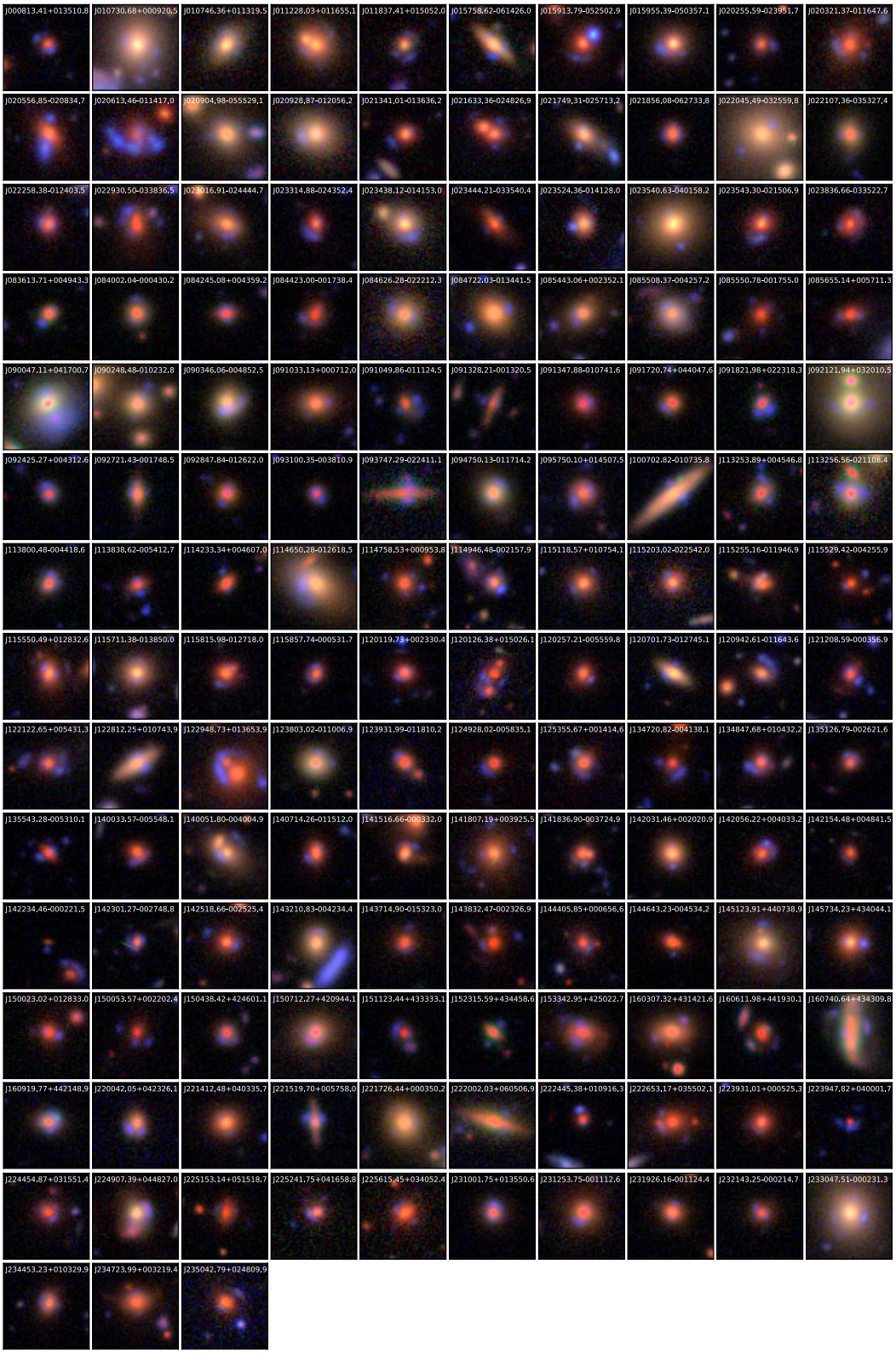

Figure B1. Images for the 143 lens candidates with grades C. All images are oriented with North up and East left.

This paper has been typeset from a TEX/LATEX file prepared by the author.